An indirectly pumped terahertz quantum cascade laser with low injection coupling strength operating above 150 K

Citation: Razavipour, S. G., E. Dupont, S. Fathololoumi, C. W. I. Chan, M. Lindskog, Z. R. Wasilewski, G. Aers, et al. "An Indirectly Pumped Terahertz Quantum Cascade Laser with Low Injection Coupling Strength Operating Above 150 K." Journal of Applied Physics 113, no. 20 (2013): 203107. © 2013 AIP Publishing LLC

As Published: http://dx.doi.org/10.1063/1.4807580

Publisher: American Institute of Physics (AIP)

Persistent URL: http://hdl.handle.net/1721.1/87016

Version: Final published version: final published article, as it appeared in a journal, conference proceedings, or other formally published context

JOURNAL OF APPLIED PHYSICS **113**, 203107 (2013)

An indirectly pumped terahertz quantum cascade laser with low injection coupling strength operating above 150 K

S. G. Razavipour,[2,a)] E. Dupont,[1,b)] S. Fathololoumi,[1,2] C. W. I. Chan,[3] M. Lindskog,[4] Z. R. Wasilewski,[1,2] G. Aers,[1] S. R. Laframboise,[1] A. Wacker,[4] Q. Hu,[3] D. Ban,[2] and H. C. Liu[5,c)]

[1]*National Research Council, Ottawa, Ontario K1A0R6, Canada*
[2]*Department of Electrical and Computer Engineering, Waterloo Institute for Nanotechnology, University of Waterloo, 200 University Ave W., Waterloo, Ontario N2L3G1, Canada*
[3]*Department of Electrical Engineering and Computer Science, Research Laboratory of Electronics, Massachusetts Institute of Technology, Cambridge, Massachusetts 02139, USA*
[4]*Division of Mathematical Physics, Lund University, Box 118, Lund 22100, Sweden*
[5]*Key Laboratory of Artificial Structures and Quantum Control, Department of Physics, Shanghai Jiao Tong University, Shanghai 200240, China*

(Received 19 March 2013; accepted 8 May 2013; published online 29 May 2013)

We designed and demonstrated a terahertz quantum cascade laser based on indirect pump injection to the upper lasing state and phonon scattering extraction from the lower lasing state. By employing a rate equation formalism and a genetic algorithm, an optimized active region design with four-well $GaAs/Al_{0.25}Ga_{0.75}As$ cascade module was obtained and epitaxially grown. A figure of merit which is defined as the ratio of modal gain versus injection current was maximized at 150 K. A fabricated device with a Au metal-metal waveguide and a top n^+ GaAs contact layer lased at 2.4 THz up to 128.5 K, while another one without the top n^+ GaAs lased up to 152.5 K ($1.3\hbar\omega/k_B$). The experimental results have been analyzed with rate equation and nonequilibrium Green's function models. A high population inversion is achieved at high temperature using a small oscillator strength of 0.28, while its combination with the low injection coupling strength of 0.85 meV results in a low current. The carefully engineered wavefunctions enhance the quantum efficiency of the device and therefore improve the output optical power even with an unusually low injection coupling strength. © *2013 AIP Publishing LLC*. [http://dx.doi.org/10.1063/1.4807580]

I. INTRODUCTION

Terahertz (THz) quantum cascade lasers (QCLs), one of the most important sources of coherent THz radiation, can cover a spectral range from ~1.2 to ~5.2 THz.[1–3] Since their invention,[4] even though many efforts have been made to improve the performance of THz QCLs in terms of operating temperature, it is not high enough to work under thermoelectric cooling systems. Recently, a design based on a three-well resonant tunneling (RT) structure, implemented in the $GaAs/Al_{0.15}Ga_{0.85}As$ material system, has reached a maximum operating temperature T_{max} of 199.5 K.[5] The limitations of RT-QCLs were addressed by Yasuda *et al.*,[6] Kubis *et al.*,[7] Kumar *et al.*,[8] and Dupont *et al.*[9] Many carriers are stationed in the injector state, ready to be transferred via resonant tunneling to the long-lived, hence heavily populated, upper lasing state (ULS). In this configuration, the bidirectional nature of resonant tunneling limits the maximum possible population inversion of RT-QCLs to 50%.[10] An efficient injector barrier must be thick enough to suppress wrong carrier injection to the lower lasing state (LLS) or other states lower than ULS and to prevent early negative differential resistance (NDR). On the other hand, it should be thin enough to reduce the tunneling time and increase the maximum current, thereby the dynamic range of the laser. The constraint on the injector barrier becomes even worse when the device lasing frequency approaches 2 THz which corresponds to a photon energy of less than 8.5 meV.[11] All the aforementioned RT-QCL issues impel designers to find novel approaches to overcome the bottlenecks of THz RT-QCL.

The majority of high-performance devices are based on RT-QCL structures.[5,12–14] In contrast, there is the indirectly pumped (IDP) scheme, well implemented in mid-IR QCL,[10] and a promising approach to improve the performance of THz QCL,[6] especially for low lasing frequencies. To date, several designs based on IDP scheme have been theoretically presented and avowed to have enough gain at higher temperatures to improve the temperature performance and overcome the fundamental limitation of designs based on RT structures.[6,15,16] Three groups have demonstrated THz structures based on the IDP scheme,[8,9,17,18] and the best performance THz QCL in terms of $k_BT_{max}/\hbar\omega$ was achieved in the $GaAs/Al_{0.15}Ga_{0.85}As$ material system by Kumar *et al.*[8]

The structures in the $In_{0.53}Ga_{0.47}As/In_{0.52}Al_{0.48}As$ material system, presented by Yamanishi *et al.*,[17–19] while not showing the highest operating temperature, exhibited advantages of a high peak output power and smooth current density-voltage (J-V) characteristics with no tunneling resonance before the designed electric field. However, the light-current

a)Electronic mail: sgrazavi@uwaterloo.ca.
b)Electronic mail: emmanuel.dupont@nrc-cnrc.gc.ca
c)Electronic mail: h.c.liu@sjtu.edu.cn

density characteristics (L-J) showed an optical power roll-over that reduces the temperature performance of the devices. It was proposed that the optical roll-over in power, might come from (i), the excess energy effect of the hot carriers in the injection region and (ii), fast tunneling rate to the next module that could frustrate the thermalization of carriers in the injector. This roll-over effect was not observable in the next generation of IDP structure with an extended tunneling time, which supports this excess energy hypothesis.[19]

Different from all aforementioned IDP designs, we are presenting an IDP four-well structure with an unusually low injection coupling strength. This new design demonstrates better performance than that of Ref. 9 in terms of the output power, threshold current density, resonance before the designed electric field, and $k_B T_{\max}/\hbar\omega$. Among all reported approaches for modeling the charge transport in THz QCL,[20–30] a simplified rate equation (RE) model, which is easy to implement and fast to compute, is employed to predict the carrier transport and estimate the optical gain in this paper. A nonequilibrium Green's function (NEGF) approach, presented in the Appendix, was used to confirm and complement the RE results.

This reported IDP four-well THz QCL is based on phonon-photon-phonon (3P) successive emissions within two neighboring thick injection barriers. Figure 1 shows the schematic energy level diagram of a 3P-QCL structure. Since both carrier injection into the ULS and extraction from the LLS are mediated by LO-phonon scattering, and since no tunneling is involved in carrier transport within a module, an efficient injection and extraction are crucial for this design, which are achieved here by wavefunction engineering through a genetic algorithm (GA). This control of wavefunctions is different from energy-band engineering and gives us an opportunity to control the desired and undesired scattering

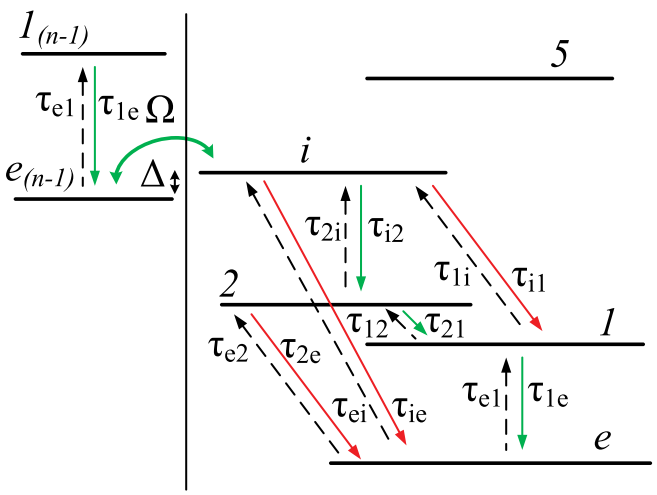

FIG. 1. Schematic diagram of a scattering-assisted QCL active region based on a phonon-photon-phonon configuration. Throughout this paper and whatever the electric field, the states within a module are labeled in energy ascending order *e*, *1*, *2*, *i*, and *5*. The solid lines show the forward scatterings, while the dashed lines indicate the back scatterings. Δ and Ω are the detuning and the coupling between states *i* and *e*, respectively. The green lines indicate the correct injection and extraction, while the red lines show the wrong injection and extraction in each module. *2* and *1* are the ULS and LLS, respectively.

rates through the shapes of wavefunctions and their relative overlaps.[31] The RE model presented in Ref. 9 is employed again during the design stage with a modified figure of merit. In Ref. 9 in order to maximize the gain in a module, a figure of merit was defined as the product of population inversion, oscillator strength, and the inverse of the superperiod length and resulted in the design of a QCL structure named V843. The design details of another THz 3P-QCL (second generation), including its specific figure of merit, will be discussed in the next section.

II. DEVICE DESIGN

A. Wavefunction engineering challenges

To understand how this scheme works, we can assume that the four-well structure consists of two phonon double wells separated by a radiative barrier. The more spatially overlapped wavefunctions in each double well lead to a faster phonon scattering process. In addition, the energy spacing of each double well should be as close as possible to the LO-phonon energy of GaAs (36.7 meV). The thickness of the radiative barrier strongly affects the oscillator strength, which, in turn, directly affects the gain and the population inversion. Even though there is no tunneling for carrier injection to the ULS and carrier depopulation from the LLS, the wrong injection and extraction channels still exist. To overcome this problem, those undesired scattering rates must be minimized to decrease the chance of the wrong injection to the LLS or non-radiative relaxation from the ULS. That is, the scattering times (red arrows in Fig. 1) must be increased. From the point of view of population inversion, the optimum structure of this scheme is a design that has a short τ_{i2} and τ_{1e} to maximize the correct injection and extraction, and second, a long τ_{i1} and τ_{2e} to minimize the wrong injection and extraction, respectively. In addition, it needs to have a fairly long relaxation time between the lasing states to keep the population inversion high enough even at higher temperatures. Therefore, in 3P structures, all four eigenenergies and their corresponding wavefunctions have to be carefully and simultaneously tailored to efficiently inject carriers into ULS and extract them from LLS. To satisfy those requirements, a GA was employed to optimize the design candidates.

Two minor issues arise when the GA is employed to find the optimum structure.

1. The fifth energy state, which was not an issue in the RT structure, may play an adverse role in 3P designs. In a conventional THz RT-QCL, the total potential across one module, which equals the sum of a THz photon energy and a LO-phonon energy, is typically less than 57 meV (considering 36 meV for LO-phonon energy and maximum 21 meV for THz photon energy[3]). In a THz 3P-QCL, this energy spacing increases to almost 90 meV so as to put the fifth energy state closer to the ULS and LLS of the previous (upstream) module at an electric field lower than the designed electric filed. This situation can substantially enhance the leakage current through tunneling to this state and decrease the population inversion. In

addition, this state can be a reason for early NDR if the injector barrier is thinned too much in order to reach a high maximum current. Moreover, as the injector state cannot be totally depleted, the dipole moment between levels *i* and *5* should be kept low in order to minimize the free-carrier absorption;[32,33] this is typically achieved by a thick radiative barrier.

2. The second issue that must be noted is the effect of tunneling between level *e* of the left module and levels *2* or *1* of the right one. If this tunneling is stronger than that of levels *e* and *i* at the desired threshold electric field, we may confront an early NDR, which could block the lasing operation of the structure or cause voltage instabilities.[34] It has been demonstrated that an IDP structure with a two-well injector can substantially reduce all resonances prior to the threshold.[18]

B. Figure of merit

Considering the aforementioned challenges, in the second generation of 3P-QCL, we targeted to maximize the ratio of the gain versus injection current at a lattice temperature of 150 K. The product of the modal gain, transit time, and inverse of the superperiod length was thus defined as the figure of merit, the details of which are provided in Ref. 35. A GA was employed to optimize the design candidates. The three-dimensional doping concentration, the injector barrier, the desired electric field, and the material ($GaAs/Al_{0.25}Ga_{0.75}As$) were fixed while the quantum well and barrier widths were free to change. The electron temperature was assumed to be 50 K higher than the lattice temperature for all subbands. Even though only the LO-phonon scattering was included in the GA process, the electron-LO-phonon, electron-impurity, and interface roughness (IR) intersubband scatterings are considered in all simulation results presented in this paper. As shown in Fig. 1, both forward and backward scattering channels were computed in our design. The quantum wells and barriers of the converged solution from the GA program are (starting with the injector barrier): **44**/64.5/**16.2**/71.5/**27.9**/104.45/**6**/49.65 Å, where the bold font indicates the barriers. Fixing the 3D doping of the structure and obtaining the quantum wells and barriers widths determine the superlattice length and the two-dimensional doping concentration. The first well after the injection barrier was delta-doped with Si to $n_s = 3.45 \times 10^{10}\,cm^{-2}$ near the center. This structure was grown by molecular beam epitaxy as a wafer named V845.

The energy spacings of the first four energy states contributing in our rate equation model are 36.6, 13.9, and 30.3 meV at 21 kV/cm, respectively. The oscillator strength and the injection coupling strength of this structure are lower than those of V843. Such a low tunnel coupling ($\hbar\Omega = 0.85$ meV at 21 kV/cm) makes the transport through the injection barrier incoherent and limits the maximum current in the lasing regime. This low value of tunnel coupling strength is attributed to the specifically defined figure of merit, whose target is to maximize the modal gain over the current ratio. Both the threshold current and the maximum current are lower than those of V843. The energy spacing of 36.6 meV between levels *1* and *e* results in a faster relaxation time of 0.21 ps at 150 K compared to 0.41 ps in V843. A longer scattering time between the lasing states (*2* and *1*) can increase the population inversion at higher temperatures. This result is achieved by the spatially separated wavefunctions of the lasing states of the structure. The conduction band diagram and squared wavefunctions of the corresponding energy states in two adjacent modules at 21 kV/cm are shown in Fig. 2. Since we have defined a specific figure of merit to find a structure with higher gain at lower current and also forced the algorithm to set the injector barrier thickness at 44 Å, the two minor issues, presented in Sec. II A, may not affect our optimization process. If we decrease the thickness of the injector barrier and enhance the coupling strength between levels *e* and *i* to reach a high current dynamic range and operating temperature, the effect of the fifth energy state and tunneling before the threshold should be considered. In this paper, both four and five-level RE were implemented and the simulation results were almost the same, suggesting the 5th state of this design has a marginal impact on transport.

C. Rate equation modeling assumptions

In this section, we present the assumptions of the RE model used for the calculations of the coherence term,

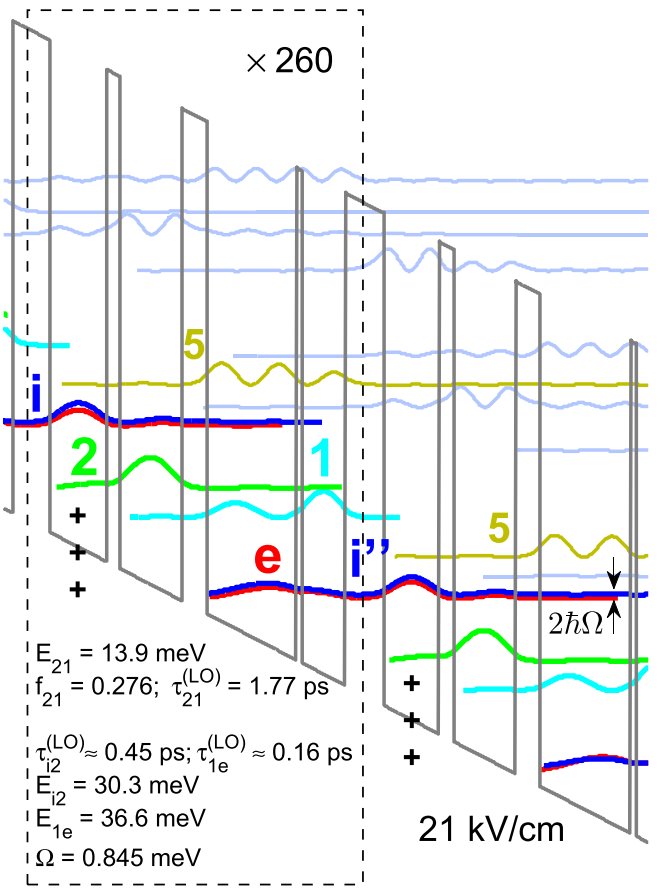

FIG. 2. Conduction band diagram and the moduli squared of wavefunctions of the THz 3P-QCL, V845, at 21 kV/cm. The "+" signs denote the position of Si doping in each module. The intersubband lifetimes by LO-phonon emission are given at the resonant in-plane kinetic energy.

tunneling time, dephasing rate during tunneling and optical transition. The RE model is based on the density matrix formalism and it is computationally very efficient. However, unlike a full density matrix model, the RE model greatly simplifies the expression of the coherence term between two tunneling states, ρ_{ab}, by involving only the coupling strength $\hbar\Omega_{ab}$, detuning energy $\hbar\Delta_{ab}$, dephasing time $\tau_{\parallel ab}$, and populations (ρ_{aa} and ρ_{bb}) of this particular pair of states a and b

$$(\Delta_{ab} - \jmath\tau_{\parallel ab}^{-1})\rho_{ab} = \Omega_{ab}(\rho_{aa} - \rho_{bb}). \quad (1)$$

The model ignores that the coherences can be interlinked: for instance, when two states b and c are coupled to the same state a by tunneling, a coherence term ρ_{bc} develops and also intervenes in the expression of ρ_{ab}. This simplification ignores the indirect resonances between states that are two modules apart.[34] Our RE model for transport is a simplified version of the one described in chapter 7 of Ref. 36 in the sense it is based on first-order resonant tunneling and it does not solve self-consistently the electronic temperature and the coupled Schrödinger-Poisson equations.

All tunneling channels between two neighbor modules were calculated based on a first-order approximation and included in our RE model. In the first-order approximation, the tunneling time between the extractor and injection states is defined as a Lorentzian function of the detuning energy, $\tau_{\text{tun}} = (1 + \Delta^2\tau_{\parallel ei}^2)/2\Omega^2\tau_{\parallel ei}$, where $\hbar\Delta$ is the energy detuning between the two extractor and injection states. The tunneling rate depends sensitively on the dephasing time, easily obtained by $\tau_{\parallel ei} = (\frac{1}{\tau^*} + \frac{1}{2\tau_e} + \frac{1}{2\tau_i})^{-1}$. It consists of lifetime terms $(\frac{1}{2\tau_e} + \frac{1}{2\tau_i})$ due to intersubband scattering and a component commonly named the "pure" dephasing time $(\frac{1}{\tau^*})$ due to intrasubband scattering. By calculating each individual broadening that comes from different scattering mechanisms, the total broadening (Γ_{tun}) will be determined by having $\Gamma_{\text{inter}}^{e(i)} = \sum_m \Gamma_{\text{inter}}^{m-e(i)}$ and $\Gamma_{\text{intra}}^{ei} = \sum_m \Gamma_{\text{intra}}^{m-ei}$, where m denotes a specific scattering mechanism, and using $\Gamma_{\text{tun}}^{ei} = \frac{1}{2}\Gamma_{\text{intra}}^{ei} + \frac{1}{2}(\Gamma_{\text{inter}}^{e} + \Gamma_{\text{inter}}^{i})$.[37] A pure dephasing time was obtained by calculating the intrasubband scattering between levels e and i at an electric field right before the two states were aligned ($\tau^* = 2\hbar/\Gamma_{\text{intra}}^{ei}$). A constant pure dephasing time of 0.2 ps was employed for all temperatures to calculate the tunneling time between e and i. This value of 0.2 ps was estimated by including the intrasubband interface roughness ($\hbar/\Gamma_{\text{intra}}^{\text{IR}-ei} \sim 0.25$ ps) and impurity ($\hbar/\Gamma_{\text{intra}}^{\text{ION}-ei} \sim 0.18$ ps) scatterings in our model and using the aforementioned equations.

In this paper, we did not model the bandwidth, $\Delta\nu$, of the gain. The peak gain of the design was simply written as

$$g_{\text{peak}} = \frac{q^2 f_{21}}{2m^*\epsilon_0 n_r c} \times \Delta N_{21}^{3D} \times \frac{C}{\Delta\nu}, \quad (2)$$

where C is a normalization constant of the gain profile, i.e., $1/\pi$ for a Lorentzian (assumed in most cases) or $\sqrt{\ln 2/\pi}$ for a Gaussian, f_{21} is the oscillator strength between the lasing states, ΔN_{21}^{3D} the population inversion 3-D density averaged over one superperiod, m^* is the effective mass in GaAs. Since we decided to keep the bandwidth as an unknown parameter, in reality throughout this work, we only modeled the product between peak gain and bandwidth, $g_{\text{peak}} \times \Delta\nu$ (gain-bandwidth product).

D. Evaluation of selected design

To investigate the effectiveness of our wavefunction engineering, the scattering times between the five states in one module, included in our RE model, and the tunneling rate between two modules, should be calculated. The following parameters were calculated: the scattering times among the first five states in one module, the population of each state, the current density, and the gain-bandwidth product based on the rate equation model at each electric field, starting from 0.5 kV/cm to 23 kV/cm at different operating temperatures. Figure 3 shows the simulation results at two electron temperatures: 70 K (lattice temperature = 20 K) and 200 K (lattice temperature = 150 K) versus electric field.

The most relevant time constants are shown in Fig. 3(a) for $T_e = 70$ K, where τ_i is the lifetime of the injection state and τ_{tun} is the tunneling time between level e and i. The variables $\tilde{\tau}_{2\text{eff}}$, $\tau_{\text{tr}}^{<}$, and $\tau_{\text{tr}}^{<}$ are the *modified* effective lifetime,

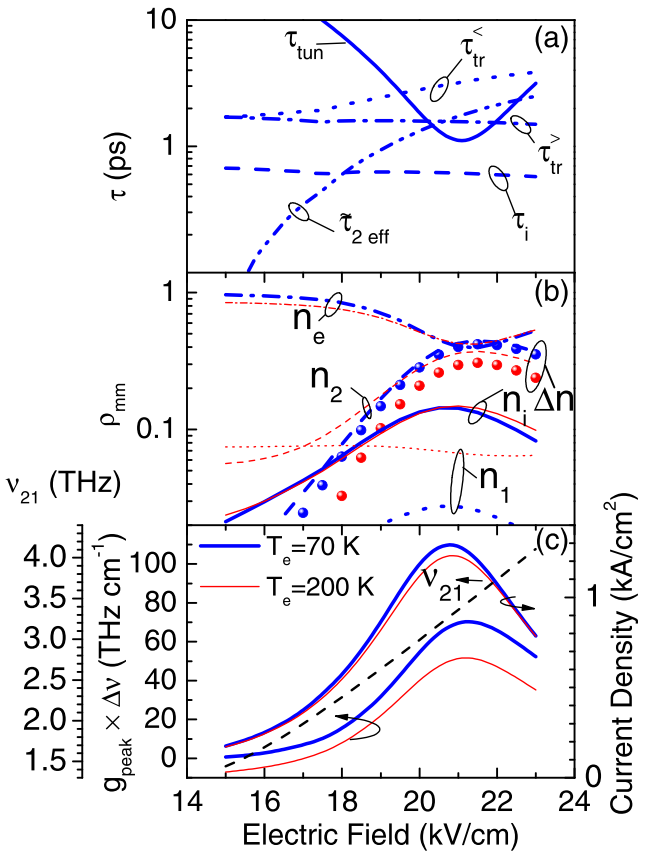

FIG. 3. The 4-level RE simulation results of the structure presented in Fig. 2. (a) Different characteristic times at 20 K ($T_e = 70$ K, thick blue lines). The scattering time presented in figure are defined as follows: τ_{tun} is tunneling time (solid line), $\tau_{\text{tr}}^{<}$ (dotted line), and $\tau_{\text{tr}}^{>}$ (dashed dotted line) are the transit times—excluding the tunneling time—across the four wells before and after threshold, respectively; τ_i is injection state lifetime (dashed line); and $\tilde{\tau}_{2\text{eff}}$ is the *modified* effective lifetime (dashed dotted dotted line). (b) Normalized populations of the four states at 20 K (thick blue lines) and 150 K (thin red lines) lattice temperatures and the population inversion $(n_2 - n_1)$ at 20 K (blue solid circles) and 150 K (red solid circles), (c) Current density, lasing frequency (dashed line), and optical gain-bandwidth product vs electric field at 20 and 150 K lattice temperatures.

transit time—excluding the tunneling time—through the four quantum wells, *without* stimulated emission, and transit time—excluding the tunneling time—through the four quantum wells, *with* stimulated emission. The last three parameters are defined in Eqs. (2), (3), and (8) of Ref. 9, respectively. Since the injector barrier is thick (44 Å), and due to the specifically defined figure of merit, the coupling between the wavefunctions of level e and i is small; the tunneling between these states is incoherent. This incoherency in transport could result in carrier accumulation at level e, increasing the backfilling, specially at higher temperatures. The faster scattering from the injector state i (τ_i), compared to the tunneling time τ_{tun} shown in Fig. 3(a), under various electric fields suggests the population on the extractor state will be significantly higher than that of the injector state. $\tau_{tr}^{<}$ and τ_{tun} are longer in V845 than in V843, which is due to higher diagonality of the structure and smaller coupling strength. Therefore, the population on the extractor state, n_e, does not change very much between the two structures as $n_e \sim \tau_{tun}/\tau_{tr}^{<}$. Even though Ω is quite small, the device is not penalized dramatically because the transport by carrier hopping between two 44 Å injection barriers (i.e., when excluding tunneling) has also been slowed down by the strong diagonality. Since by design, the lifetime of the injection state, τ_i, is short, and the transit time without stimulated emission is rather long, there is no need to reach coherent transport through the injection barrier, i.e., $\tau_{tun} \ll \tau_i$. However, we would recommend to have τ_{tun} comparable to τ_i, i.e., $\tau_{tun} \gtrsim \tau_i$, to lower significantly the population on the extractor state, which can be achieved by increasing the tunnel coupling strength. At 21 kV/cm, the energy spacing between states i and 2 (E_{i2}) in V845 is 6.4 meV below the GaAs phonon energy, as a result the injection of carriers on ULS is slowed down: $\tau_{i2} \sim 0.56$ ps vs 0.33 ps for V843 at 150 K. This increase in injector state lifetime explains why n_i is even worse (i.e., larger) in V845 as $n_i \sim \tau_i/\tau_{tr}^{<}$. The current at e-i alignment, calculated as the product of $n_e - n_i$ and the inverse of τ_{tun} will be lower than that of V843 due to lower $n_e - n_i$ and higher τ_{tun} simultaneously.

Figure 3(b) shows the carrier density of each state at different electric fields. As expected, the carrier density at level e, n_e, is dominant almost over the entire bias range. This shows that most of the carriers are piled up at level e, even near the designed electric field of 21 kV/cm. The same effect of carrier accumulation on level e is predicted by NEGF simulations (see Appendix). Consequently, due to the backfilling from level e, the density of carriers at level *1* (LLS) increases dramatically when the temperature increases from 20 K to 150 K. The population inversion (solid circles) decreases when the temperature varies from 20 K to 150 K but it is still higher than that presented in Ref. 9 due to a longer *modified* effective lifetime $\tilde{\tau}_{2eff}$. At lower temperatures since the backward scattering is not fast, level *1* is almost empty.

The gain-bandwidth product, current density, and lasing frequency are shown in Fig. 3(c). The value of the gain-bandwidth product changes modestly, from 20 K to 150 K. The maximum value of the gain-bandwidth product is 60.4 THz cm^{-1} at 20 K, while it decreases to 48.1 THz cm^{-1} and 43.1 THz cm^{-1} at temperatures of 125 K and 150 K, respectively. The backfilling to the level *1* at higher temperatures, due to the piling-up at level e, is the main reason for the population inversion reduction and hence gain reduction. Even though the tunneling time τ_{tun} is exactly minimized at 21 kV/cm, i.e., at the electric field when e-i are perfectly aligned, the current density is peaked at ~20.7 kV/cm due to a decline of $n_e - n_i$ close to the resonance. Figure 3(c) shows that the lasing frequency will vary from 2.8 THz near the threshold to 3.2 THz at the electric field near the NDR by assuming the product of the gain bandwidth ($\Delta\nu$) and the cavity loss (α_{cav}) is $\Delta\nu \times \alpha_{cav} \sim 42$ THz cm^{-1}, which will be discussed in Sec. IV E.

III. EXPERIMENTAL RESULTS

The whole QCL structure V845 consists of 260 repeats of the module presented in Fig. 2 and is grown on a semi-insulating GaAs substrate using molecular beam epitaxy with a total thickness of 10 μm. The active region is sandwiched between a 100 nm of 3×10^{18} cm^{-3} bottom n$^+$ GaAs and a top stack of 40 nm of 7×10^{17} cm^{-3}, 50 nm of 5×10^{18} cm^{-3}, 10 nm of 5×10^{19} cm^{-3} n$^+$ and 3.5 nm of low-temperature (LT) grown GaAs. The first layer of the top stack is meant to adjust the Fermi level so as to align with the injector state of the first module, and the last two layers are used to form a non-alloyed ohmic contact.

We should point out that this V845 wafer was grown using a nearly depleted Ga cell. Indeed, the cell ran out of gallium during the flux measurement procedure conducted on the next day. Since the evaporation in such a situation is often taking place from several remaining droplets of gallium, the evaporation surface area can change in a random fashion. Thus, despite attempt to stabilize the flux by appropriate ramp of the cell temperature during the growth, the average Ga flux decreased by more than 2% during the active region deposition, while the analysis of X-ray Diffraction (XRD) data revealed step-like changes in the Ga flux which resulted in three distinct regions of different periodicity: the main region with 1.4% shorter period than the target value, and the other two regions with about 30 repeats each in which the periods were 0.4% shorter and 0.6% longer than the target value.

Two different fabrication processes were employed to compare the effect of waveguide loss on device performance of this structure. Since the oscillator strength of this 3P structure is lower than that of V843, the maximum operating temperature may be enhanced more substantially by lowering waveguide loss.[34,38] The first fabrication process, device A, used a Au-Au ridge waveguide with a 144 μm width and 1.07 mm length, while the second fabrication process, device B, has a wider (159 μm) and longer (1.79 mm) waveguide. In addition, the 100 nm thick top contact layer was removed to lower the waveguide loss. The Ti/Au metalization process and In-Au bonding technique were employed for device A, while device B was fabricated using a Ta/Au metallization process and an Au-Au bonding process.

Figure 4(a) shows the pulsed light-current density-voltage (L-J-V) characteristics of device A from 10 K to 128.5 K, with a pulse duration of 250 ns and repetition rate

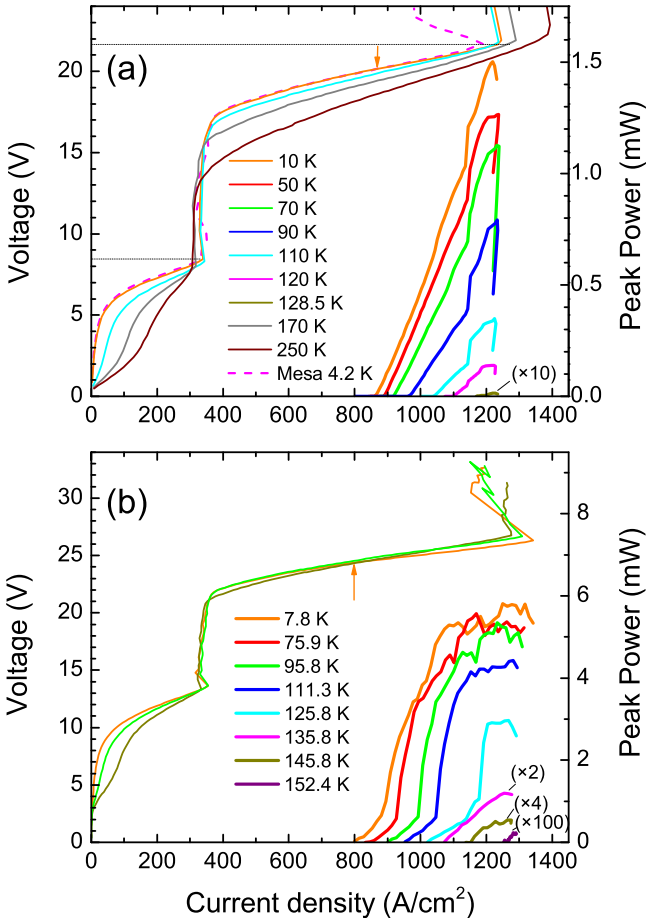

FIG. 4. Left axis: The bias voltage of THz 3 P-QCL V845 versus the current density, (a) device A (b) device B. The short vertical arrows show the change in the slope of the V-J curves at laser threshold and the lowest temperature (10 K for device A or 7.8 K for device B). Right axis: Collected THz light (optical output power) versus current density at different heat sink temperatures. Since the measurement set-up and the waveguide properties are different, the collected light, the maximum current density, and the threshold current are different in plots (a) and (b). Drop voltage on device B is higher than on device A, the latter having the top 100 nm n^+ contact GaAs layer hence, a top Schottky contact with a short depleted region (~18 nm).

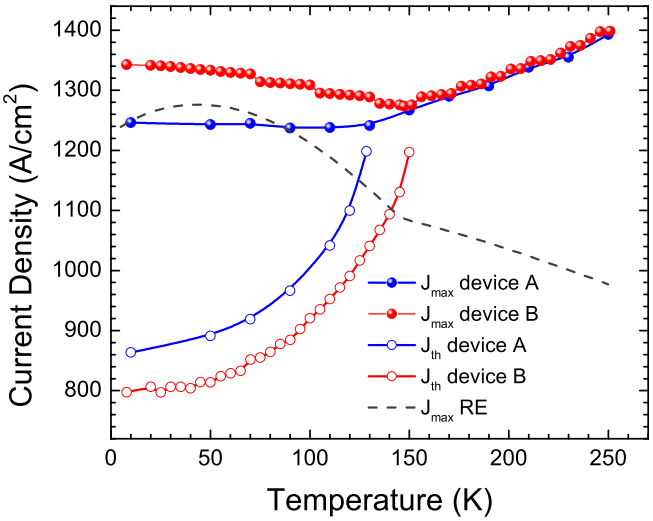

FIG. 5. Maximum current density and threshold current density as functions of heat sink temperature for devices A and B. The dashed line shows the result of a 5-level rate equation simulation assuming a constant product $\Delta\nu \times \alpha_{cav} = 42\,\mathrm{THz\,cm^{-1}}$.

of 1 kHz. The threshold current density of 0.87 (0.8) kA/cm^2 was measured for device A (device B) package, while the maximum current density was 1.25 (1.34) kA/cm^2. The lower cavity loss results in a lower threshold current density (i.e., 0.8 kA/cm^2 at 7.8 K for device B vs 0.87 kA/cm^2 for device A at 10 K) and a higher maximum current density which enhances the dynamic range of device B and improves the maximum operating temperature. The maximum operating temperatures of 128.5 K and 152.5 K were achieved with devices A and B, respectively. The maximum collected optical power in devices A and B was 1.5 mW and 5.8 mW at lattice temperature of 10 K and 7.8 K, respectively (The optical set up and the injected electric power were different in devices A and B).

The solid orange V-J curve (device A) in Fig. 4(a) shows the first NDR at 8.5 V and the final NDR at 21.8 V. By considering a 0.75 V Schottky drop voltage from the top contact,[39] we will reach 21.05 V as the main NDR of the design, which nicely matches with our design electric field (21 kV/cm). The first NDR at 8.5 V (7.75 kV/cm) comes from the resonance tunneling between levels e and 1. The Schottky drop voltage of top contact can be accurately obtained by comparing the V-J measurements of the lasing and non-lasing devices. The width and length of the non-lasing device were reduced to 248 μm and 174 μm, respectively, to increase the loss of the cavity, hence suppress the stimulated radiation. In addition, the non-lasing device was annealed to form PdGeTiPtAu ohmic contacts, which had the advantage—for this particular application—to increase the waveguide loss.[39] Besides, these ohmic contacts reduce the potential drop across the metal/semiconductor interfaces and help to achieve accurate V-J curve measurements. The dashed-magenta curve in Fig. 4(a), showing the V-J characteristic of the non-lasing device, is also plotted, and the difference between the V-J curves of the lasing and non-lasing devices becomes distinguishable only after the threshold voltage indicated by a vertical arrow. The dashed-magenta curve was shifted upward along the voltage axis by a Schottky drop voltage of 0.75 V so as to overlap with the lasing V-J curve of the device A. At the NDR, the difference in current density between the lasing ridge and the non-lasing mesa is small, only ~60 A/cm^2. We also note that, above 130 K, a small resonance in the J-V characteristics develops slightly above 2 V. As shown in Fig. 5, the maximum current density (J_{max}) of both devices A and B slightly decreases from 8 K to a temperature close to T_{max}. This reduction of current density is 10 A/cm^2 from 10 K to 110 K in device A and 70 A/cm^2 from 7.8 K to 145.8 K in device B. Above 110 K for device A, or 145.8 K for device B, the J_{max} starts to increase slowly. Above 150 K, the J_{max} of devices A and B are very similar since both devices are not lasing anymore. At a high temperature of 250 K, the J_{max} of device A is only ~150 A/cm^2 higher than at 10 K.

The light measurement of device A shows that the maximum amount of the light was collected at a current density near the NDR. The roll-over of output optical power in current ranges below maximum currents, observed in Ref. 18,

does not exist in our device. Since, on the one hand, the coupling injection strength of our device is lower than that of the one presented in Ref. 18 (0.85 meV compared to 2 meV), and on the other hand, the excess energy (voltage drop per module minus $2E_{LO}$) of our device is low (7.3 meV at design electric field that could compensate for the small injection energy E_{i2}), our device does not suffer from the roll-over effect that can degrade the performance of THz IDP-QCL.

The spectral measurements of this structure at different current injections and different temperatures are illustrated in Fig. 6. At 10 K, the lasing frequency started from ~2.4 THz at near threshold voltage and blue-shifted to ~2.8 THz at 21.7 V considering the highest amplitude longitudinal mode. At a current injection of 1.25 kA/cm^2, corresponding to 21.7 V, the structure acts as a multiple-wavelength source that lases from 2.32 THz to 2.94 THz at 10 K. Even though the Schrödinger equation helped us to estimate the lasing frequency of the first generation of 3P-QCL, it cannot predict the spectrum of V845 accurately. For comparison, the simulations (the dashed line in Fig. 3(c)) predict that the lasing frequency is 2.9 THz at 19.7 kV/cm (an actual device bias of 20.45 V); experimentally, 2.4 THz was observed. At 21 kV/cm, the lasing frequency is 3.36 THz (simulation) vs 2.32–2.94 THz (experiment). At 150 K and near the J_{max}, the spectral measurement shows a single lasing frequency of ~2.4 THz, which seems to be the dominant frequency range (2.4–2.5 THz) over the lasing operating temperatures.

The theoretical study of laser frequency versus bias and temperature is beyond the scope of this paper. We will mention only three mechanisms that can change the peak gain frequency, and which were not taken into account in our RE model. Many-body interactions, in particular the depolarization (intersubband plasmon), can red-shift the optical resonance in an inverted two-level system.[40,41] This depolarization effect could be weak though due to the small overlap between the lasing wavefunctions. If the population on LLS is substantial, for instance at high temperature by backfilling, the occurrence of Bloch gain cannot be excluded and it would tend to red-shift the peak position.[42,43] Finally, our model does not solve self-consistently the Schrödinger, Poisson and rate equations. In reality, due to charge separation the electric field is not uniform within one module. Since the section between the expected positions of the ULS and LLS wavefunctions is more conductive when stimulated emission occurs, the electric field can be configured differently when device is lasing, thereby reducing the Stark effect on the lasing transition.[44] However, considering the small carrier concentration in THz QCLs, this effect should be weak too. We have not verified yet numerically these three hypotheses. It is worth mentioning the NEGF simulations were more successful than RE in predicting the laser frequency (see Appendix).

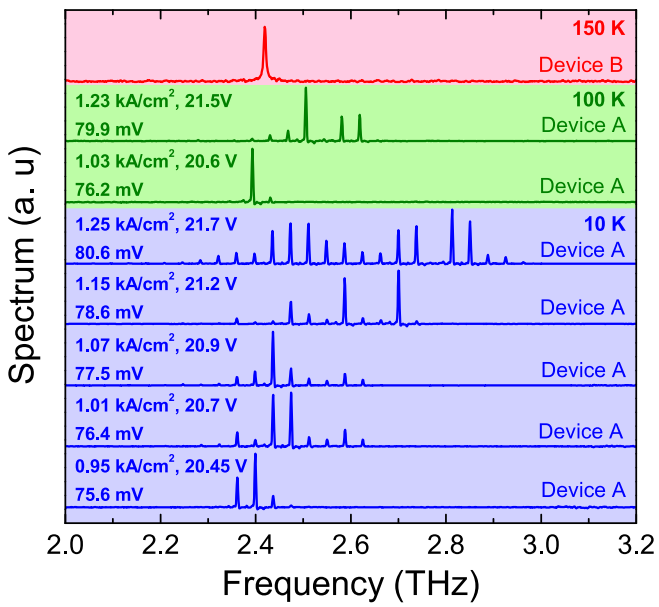

FIG. 6. THz spectra recorded for different biases and temperatures. The current density, the applied voltage bias, and voltage drop per module are reported in the figure. Spectrum at 150 K was collected from device B while all other spectra were measured from device A.

IV. RATE EQUATION ANALYSIS

A. Electrical characteristics

For the sake of simplicity, the pure dephasing time, τ^*, was left temperature independent (0.2 ps) in our rate equation-based modeling. We did not try to match for all temperatures the simulated J_{max} with the experimental values. To investigate the performance of this design, the current density of the structure in a full range of electric fields at different temperatures was calculated and the simulation results of lasing and non-lasing devices at 10 K are plotted in Fig. 7. A threshold electric field of 19.4 kV/cm was derived and matched the experimental value by assuming a gain bandwidth × cavity loss product of 38.5 THz cm^{-1}. Two pre-threshold current peaks occur before the final NDR: the effect of tunneling of states *e* to *1* and *e* to *2* aligned at

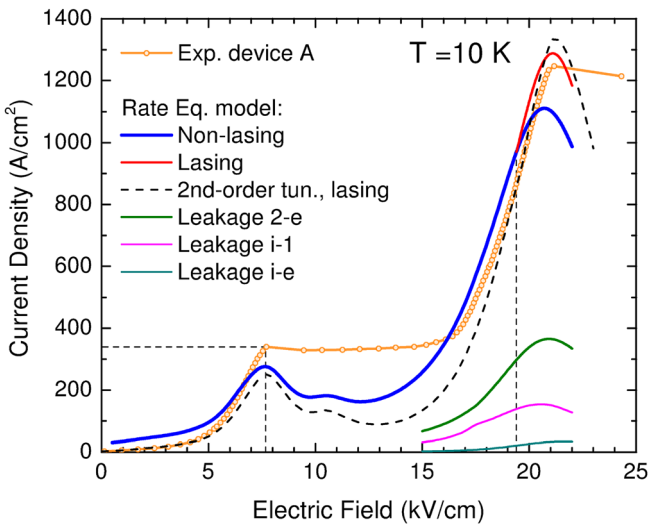

FIG. 7. The current density vs electric field were calculated by using a 5-level first-order rate equation formalism at 10 K for lasing (red) and non-lasing (blue) devices. The green, pink, and cyan lines represent the leakage currents from the wrong extraction *2-e*, and the wrong injections *i-1*, *i-e*, respectively. The vertical dashed lines were plotted to determine the first NDR and threshold voltage of the device at 10 K. The black dashed line shows the current density by using the second-order model of tunneling. The experimental curve of device A, shown as an orange dotted line, was measured at 10 K for comparison.

electric fields of 7.7 and 10.5 kV/cm, and giving rise to current peaks at ~7.7 and ~10.5 kV/cm, respectively. The current calculation with stimulated emission (red) and without stimulated emission (blue) is different after the threshold voltage. The peak current density of the lasing curve increases by ~177 A/cm^2, and is slightly shifted by +0.3 V in voltage compared to the non-lasing curve, while the two curves overlap before the threshold. From Fig. 3, two observations should be recalled: (i) above threshold, the total transit time—excluding the tunneling time—across the four quantum wells, $\tau_{tr}^{>}$, is much faster than the counterpart without stimulated emission, $\tau_{tr}^{<}$, this being mostly due to the high diagonality of the laser transition; (ii) the tunnel coupling strength is too low (0.85 meV) to ensure a coherent transport through the tunneling barrier ($2\Omega\tau_{\|ei} = 0.44$, instead of $2\Omega\tau_{\|ei} > 1$ if tunnel transport were coherent). As a result, the transport through the structure is essentially limited by the transit time within the period without stimulated emission ($\tau_{tun} \ll \tau_{tr}^{<} \approx 2\tau_{i2} + \tau_{21} + \tau_{1e}$), while the tunneling time becomes relevant with stimulated emission ($\tau_{tun} \lesssim \tau_{tr}^{>} \approx 2(\tau_{i2} + \tau_{1e})$), hence the maximum current with (without) stimulated emission will (not) be sensitive to the dephasing time, $\tau_{\|ei}$.[25] We came out with this estimation $\tau^* \sim 0.2$ ps in order to bring the simulated lasing V-J curve close to that of non-lasing and we found that it was roughly consistent with the intrasubband scattering rates by IR and e-impurity potentials (Sec. II C).

As already mentioned in Sec. II D, our 5-level rate equation model suggests a slight decrease of voltage (0.3 kV/cm in Fig. 7) at J_{max} for the non-lasing devices because of the decline of the population difference between the tunneling states, $n_e - n_i$, when these levels approach the resonance. This effect is not likely to happen on lasing devices because, above threshold, the population inversion is clamped, hence the population difference $n_e - n_i$ does not change very much above threshold and J_{max} occurs when the tunneling time, τ_{tun}, is at a minimum, i.e., when the levels *e* and *i* are aligned (21 kV/cm).[45] This voltage shift effect for non-lasing devices would not be easy to measure experimentally, unless a larger coupling strength is used to empty more drastically the extractor state. Recently, the electrical characteristic of a non-lasing device from a wafer with a large coupling ($\hbar\Omega = 1.54$ meV) strongly suggests that the peak current of the *e-i* channel is shifted by −1.5 V from the design voltage.[46]

The leakage current from the wrong extraction channel *2-e*, shown by a green line in Fig. 7, is lower than that of V843, as is its fractional contribution to the total current. Lower spatial overlap and higher energy spacing (50.5 meV in V845 compared to 42 meV in V843) between states *2* and *e* are the two main reasons for this lower leakage current and simply result from the specific wavefunction engineering where the net gain per electron injected was approximatively optimized through our GA approach. Two leakage currents from the wrong injection channels (*i-1* and *i-e*) were also plotted in Fig. 7. As expected, they are lower than the wrong extraction current, showing the good injection efficiency to the ULS in this IDP-QCL. The lower wrong injection could result in a higher internal quantum efficiency (longer $\tilde{\tau}_{2eff}$) and hence a higher output optical power.

The observed small shoulder in the J-V curves around 2 V that slowly develops above 130 K (Fig. 4(a)) is related to tunneling between levels 2_{n-1} and i_n and is very well simulated by the NEGF model (see Fig. 11 in the Appendix for NEGF simulated J–V at high temperatures). At such high temperatures, level *1* is more populated and the channel $1 \rightarrow i$ (resonant at ~6.6 kV/cm) is more activated, which, when combined with the $e \rightarrow 1$ channel (resonant at 7.7 kV/cm), results in slightly shifted, slightly less intense and broader peaks of the J–V characteristics (lower conductance) before the first NDR. Such alterations of the electrical characteristics before the first NDR have been experimentally observed here at high temperatures. The non-vanishing current below the *e-1* resonance comes from the first-order approximation of tunneling and a good fit was obtained in this voltage range by using the second-order approximation of tunneling (black dashed line in Fig. 7).[47]

B. Maximum current density versus temperature

When the RE model is employed with a constant pure dephasing time τ^*, a constant product $\Delta\nu \times \alpha_{cav}$, and five states (including the different scatterings between them), the simulated maximum current density stays roughly constant up to 85 K (with even a slight increase below 45 K) and then decreases more rapidly with temperature due to back scattering, whereas the experiment shows a reduction in J_{max} as devices are lasing (Fig. 5). The result of this simulation is plotted as a dashed line in Fig. 5. For a constant product $\Delta\nu \times \alpha_{cav} = 42$ THz cm^{-1}, the back scattering, simulated by RE model, would result in a reduction of J_{max} by ~260 A/cm^2 from 10 to 250 K, which is contrary to the experimental observation of an increase ~150 A/cm^2 over the same temperature range. For a phonon population in thermal equilibrium at 250 K, the different scatterings involving the fifth state result in a 4% raise in the simulated J_{max}, which is insufficient to compensate the back scattering effects.

Since on the one hand, the J_{max} of devices A and B decrease with temperature until the laser effect dies and eventually match their values close to and above the highest T_{max}, and on the other hand, the increase in current is unambiguous above T_{max}, this could suggest that two (or more) mechanisms are involved in the temperature dependence of J_{max}, for instance a mechanism specific to transport in the lasing regime, and another one specific to transport at high temperatures. The disagreements between experiments and RE simulations as shown in Fig. 5 are not well understood yet. The same behavior in maximum current density was also observed by NEGF simulations (see Appendix). The discrepancies may come (i) from employing a constant product $\Delta\nu \times \alpha_{cav}$ while this parameter might increase with temperature, (ii) from assuming a constant pure dephasing time while this parameter could decrease with temperature, thereby affecting the J_{max} in the lasing regime, and (iii) from omitting several possible leakage mechanisms, such as the excitation to the fifth level by reabsorption of nonequilibrium optical phonons[48–51] followed by thermionic emission to the continuum.[50]

The initial raise of the simulated J_{max} at low temperature is related to the energy gap between levels *i* and *2* that is

6.4 meV smaller than the phonon energy; however, if the subband i is more populated at high momentum than the assumed Boltzmann distribution, the increase of J_{max} (and gain too) at low temperature would partially—if not completely—disappear. Modeling accurately the maximum current density, in particular its temperature dependence, is the subject of intense research in order to understand all aspects of transport in THz QCL.[48,50,52,53]

C. Intermediate resonances

At low temperature, there are two important anticrossing resonances before the main resonance between states e and i. Since both simulated current peaks at electric fields of 7.7 and 10.5 kV/cm are far less than the threshold current, the two pre-threshold tunneling resonances (*e-1* and *e-2*) impose a minimum impact on device lasing performance. This calculation should be performed for all structures based on the 3P scheme to make sure the currents at resonances of e to *1* and e to *2* are substantially lower than the threshold current, without sacrificing the dynamic range of the laser. To show how the wavefunctions couple when the leakage current density due to the *e-1* tunneling resonance is peaked, the conduction band diagram of V845 is calculated and plotted in Fig. 8. The lowest energy state of the left module (e_{n-1}) is in resonance with the second energy state of the right module (1_n) at an electric field of 7.7 kV/cm, which is lower than the threshold electric field. The coupling strength between these states is $\hbar\Omega_{e1} = 0.235$ meV. Since the tunneling between level e and *1* is incoherent ($4\Omega_{e1}^2\tau_{\|e1}\tau_1 = 0.35$ at 20 K), the dephasing time constant can affect the tunneling current.[8,25] The carriers passing through the injector barrier (tunnel from e_{n-1} to 1_n) will be relaxed to the next extraction state (e_n). The second resonance should be observed at 10.5 kV/cm, where the states e and *2* are aligned. For this resonance, the transport is clearly incoherent, with a low coupling strength between the states e to *2* ($\hbar\Omega_{e2} = 0.147$ meV) and a short relaxation time of level *2* ($\tau_{2e} = 0.25$ ps) that result in very low coherence in tunneling ($4\Omega_{e2}^2\tau_{\|e2}\tau_{2e} \sim 6\times10^{-3}$ at 20 K). Therefore, the current through the *e-2* channel is smaller than that of *e-1* channel because of its smaller coupling strength and, to a lesser extent, due to its shorter dephasing time. We note that the relaxation times of levels *2* and *1* are inverted at these low electric fields, i.e., fast for level *2* (0.18 ps) and slow for level *1* (3.48 ps) as the two lasing states did not anticross yet (*2* and *1* are aligned at 13.3 kV/cm).

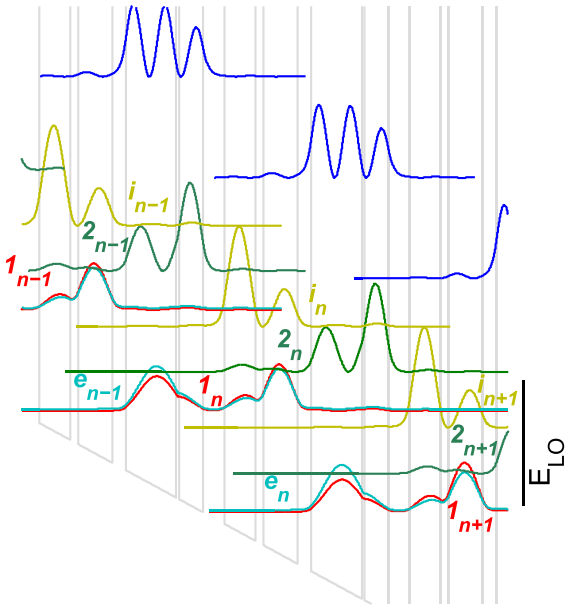

FIG. 8. Conduction band diagram and the moduli squared of wavefunctions of V845 at 7.7 kV/cm. States in left module (upstream), middle module, and right module (downstream) are represented by subscripts $n-1$, n, and $n+1$, respectively. The extraction state (e) of each module is in resonance with state (1) of next module at an electric field of 7.7 kV/cm.

The measured peak leakage current at the first NDR, i.e., 7.7 kV/cm, is $J_{res} = 340\,A/cm^2$, while the simulation result is 276 A/cm^2. Even though the maximum current density of the lasing device can be reasonably well predicted by our simulation (at least at low temperature), the experimental value of J_{max} on the non-lasing device is 78 A/cm^2 higher than our simulation result. A similar vertical shift (64 A/cm^2) was also observed in the peak leakage current density at 7.7 kV/cm (340 A/cm^2 measured value vs a 276 A/cm^2 simulation result). The ratio of the maximum current over the resonance peak current before threshold (J_{max}/J_{res}) at 10 K in V845 is slightly better than that of V843 (3.7 in V845 compared to 3.1 in V843), due to the weaker *e-2* resonance in V845 because of the wider radiative barrier ($\hbar\Omega_{e2} = 0.147$ meV in V845 vs 0.24 meV in V843).

D. Differential resistance at threshold

The differential resistance of lasing device A (at different temperatures) versus current density, plotted in Fig. 9, shows a clear discontinuity at the laser threshold, whereas the same parameter is displayed as a smooth curve (dashed-magenta line) for the non-lasing mesa device (shown only at 4 K). The ~16% fractional change of differential resistance at threshold, observed in measurement at 10 K, is lower than what the rate equation model predicts (32% extracted from

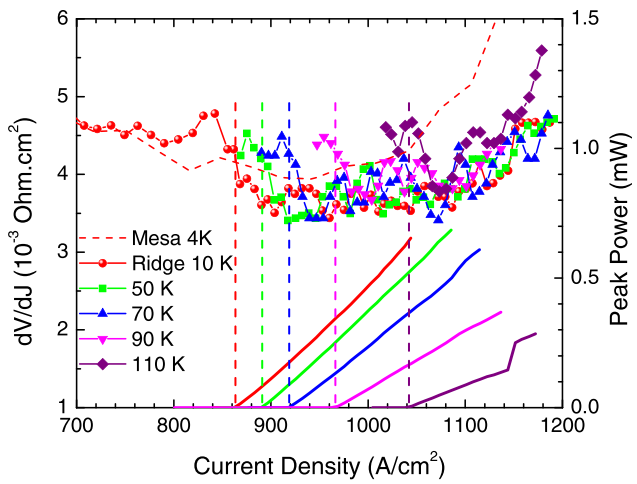

FIG. 9. Left axis: The differential resistance of non-lasing (the red dashed line) and lasing (solid lines with symbols) device A versus current density at different temperatures. The L-J measurement results are also plotted (right scale) to determine the threshold current at each temperature.

Fig. 7 by assuming $\Delta\nu \times \alpha_{cav} = 38.5\,\mathrm{THz\,cm^{-1}}$). To more accurately determine the position of the discontinuity which shifts to higher currents with temperature, the L-J curves of device A are plotted with vertical dashed lines to denote the corresponding threshold points. A better internal efficiency of the second generation of THz 3P-QCL due to the longer *modified* effective lifetime of the ULS and shorter lifetime of the LLS results in a clear discontinuity of differential resistance and a higher output power (1.5 mW in device A compared to 0.8 mW in Ref. 9 with the same collecting optics). In Ref. 9, the discontinuity of differential resistance was estimated and appears to depend on two relaxation times associated with the extractor state, the wrong extraction lifetime (τ_{2e}), and the depopulation (τ_{1e})

$$\frac{\Delta R_{th}}{R_{th}} = \Delta\rho_{th}\frac{\tau_{2e} - \tau_{1e}}{\tau_{2e} + \tau_{1e}}, \tag{3}$$

where $\Delta\rho_{th}$ is the normalized population inversion at threshold. The discontinuity of differential resistance in V845 is improved compared to the first iteration 3P design (V843) in a two-fold strategy: (i) τ_{2e} is longer because of the thicker radiative barrier ($\tau_{2e} = 5.6$ vs 2.55 ps in V843 at electron temperature of 70 K) which results in a higher *modified* effective ULS lifetime and (ii) τ_{1e} is shorter due to the higher energy spacing to make the depopulation more efficient. The observation of a discontinuity in differential resistance on V845 tends to support our hypothesis about the vanishing discontinuity on V843, which was attributed to a slow depopulation rate as the energy spacing between the states *1* and *e* was 9 meV below the LO-phonon energy.[9] This discontinuity in differential resistance on V845 is consistent with the higher emission power from this wafer, since $\Delta R_{th}/R_{th}$ is closely related to the internal efficiency of the QCL.

E. Cavity loss estimation

Even though this RE model is not very accurate, for instance in predicting J_{max}, it was used here for estimating the product between the gain bandwidth, $\Delta\nu$, and the cavity loss, α_{cav}. Figure 10 shows the simulated $\Delta\nu \times \alpha_{cav}$ as a function of lattice temperature. The gain of the structure was calculated at all electric fields and different temperatures and the cavity loss and/or the gain bandwidth were adjusted to match the simulated and experimental voltage thresholds. Simulations were performed under two conditions: (i) the electron temperature is 50 K($\equiv\Delta T_e$) higher than lattice temperature, (ii) the electron temperature is 100 K higher than lattice temperature. By having the voltage threshold of device A at different temperatures (the experimental results range from ~19.4 V at 10 K to 20.5 V at 128.5 K after substration of the Schottky barrier) and mapping the gain value at each temperature, a product $\Delta\nu \times \alpha_{cav} \sim 42\,\mathrm{THz\,cm^{-1}}$ was inferred for $\Delta T_e = 50$ K. This inferred value remains almost constant (~$42\,\mathrm{THz\,cm^{-1}}$) at temperatures of 50-120 K, but slightly drops to ~$38.5\,\mathrm{THz\,cm^{-1}}$ at 10 K. This drop is likely attributed to the underestimated gain calculation at lower temperatures because the slow-down in carrier injection from level *i* to *2* at low temperatures (e.g., below 20-30 K) might be exaggerated in the modeling. This underestimation of the gain leads to a lower inferred cavity loss. Indeed, especially at low temperatures, the injection of carriers into the ULS is very sensitive to the actual electron distribution of carriers in the injector subband as the energy spacing E_{i2} is fairly detuned from the phonon energy (7.45 meV at 19.4 kV/cm, the threshold electric field at 10 K); in other words, the Boltzmann distribution with a characteristic temperature of 60 K (used for the simulation at 10 K lattice temperature) might be too far from reality.

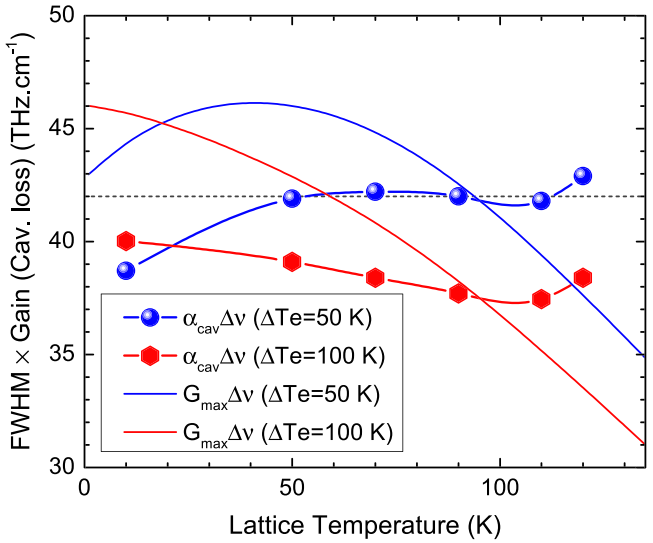

FIG. 10. Symboled lines are the cavity loss × gain bandwidth products of device A, calculated by a 4-level RE model, at different lattice temperatures (T_L) and for two electron temperatures, T_e, such as $T_e - T_L = 50$, 100 K. The solid lines are the peak gain × gain bandwidth products vs lattice temperature at 19.7 kV/cm calculated by the RE model.

It is worth mentioning that the inferred product $\Delta\nu \times \alpha_{cav} \sim 42\,\mathrm{THz\,cm^{-1}}$ is for an assumed Lorentzian gain profile ($C = 1/\pi$ in Eq. (2)); if a Gaussian gain spectrum had been chosen, this value would be multiplied by 1.48 ($62\,\mathrm{THz\ cm^{-1}}$). Close to T_{max} of device A, the peak gain and bandwidth simulated by NEGF are $33\,\mathrm{cm^{-1}}$ and 1.56 THz, respectively (see Appendix), resulting in a product of $51.5\,\mathrm{THz\,cm^{-1}}$, in agreement with the estimation from the RE model ($42\text{-}62\,\mathrm{THz\,cm^{-1}}$). Under the second condition, when the electron temperature is 100 K higher than the lattice temperature, the derived $\Delta\nu \times \alpha_{cav}$ decreases with temperature which is unlikely to happen.[13] This behavior is due to a too fast degradation of the gain versus temperature when $\Delta T_e = 100$ K as this assumed temperature difference probably overestimates the carrier distribution at high momentum in the subbands. Globally, it seems the heating is less than 100 K.[54] Repeating the same exercise with the lasing device B, a lower $\Delta\nu \times \alpha_{cav}$ product of ~$38\,\mathrm{THz\,cm^{-1}}$ (with Lorentzian profile) was estimated for this waveguide, which is consistent with previous reports.[5,13,55]

V. CONCLUSION

In this paper, we present a THz indirectly pumped QCL based on phonon-assisted injection and extraction. A simple rate equation formalism was employed and a genetic

algorithm was used to optimize the structure to have the maximum gain while keeping the current injection as low as possible. The product of net optical gain and transit time was defined as a figure of merit to be maximized at the lattice temperature of 150 K in the design optimization process. The fifth energy state was engineered to be far from the first four states and makes sure its carrier density is negligibly low.

Based on the design optimization, the second generation of THz 3 P-QCL was demonstrated and a higher dynamic range ($(I_{max} - I_{th})/I_{max} = 0.3$ (0.4) in device A (device B) compared to 0.24 in V843), higher operating temperature (152.5 K compared to 138 K (Ref. 56)) and lower lasing frequency (2.4 THz at 150 K compared to 3.2 THz at 138 K) were obtained. The lower loss waveguide plays an important role in pushing the maximum temperature to 152.5 K and a high performance THz QCL with $k_B T_{max}/\hbar\omega = 1.3$ was demonstrated. Despite these improved performances, the intrasubband scattering contribution to the dephasing of the tunneling process has been identified as a crucial parameter, which limited the dynamic range of this device. Therefore, future optimization schemes should include a realistic model of the tunnel dephasing and linewidth of the lasing transition.

To further improve the performance of THz 3P-QCL, one can design a structure with a thinner injector barrier to increase the gain and maximum current. A higher injection tunnel coupling strength might be tolerable as long as the early NDR, here observed at 7.7 kV/cm, can effectively be suppressed. As a result, the lasing dynamic range can be expanded and the maximum lasing temperature could be further enhanced. Inserting one more quantum well in the upstream phonon double well could effectively minimize the leakage current arising from tunneling resonances prior to lasing threshold.[11] In such QCL structures, a higher injection tunnel coupling strength might, therefore, be chosen to further improve device performance.

It is fair to recall the other very efficient—and experimentally proven—strategy to suppress the early NDR, which employs a design of a two-state extractor.[18,19,57] This solution would imply dealing with five and possibly six levels per module because the third state of the double-well extractor will likely be close in energy with the lasing states. In such a case, this third state should be employed in the depopulation mechanism via tunneling, resulting in the abandonment of the "3P" nature of the designs we have explored because a two-level extractor IDP-QCL would work according to a 2PTP sequence (phonon-photon-tunnel-phonon) between two injection barriers.

The main message conveyed by this paper is to demonstrate that, despite its disarming simplicity, the 3P-QCL device can be optimized in some sophisticated ways and perhaps, could reach performances suitable for practical applications.

ACKNOWLEDGMENTS

The authors thank Dr. Marek Korkusinski from NRC for providing the genetic algorithm and Pietro Patimisco from the Università and Politecnico di Bari for helpful stimulating discussions. They also would like to acknowledge the financial supports from Natural Science and Engineering Research Council (NSERC) of Canada, Canadian Foundation of Innovation (CFI), the CMC Microsystems, and Ontario Research Fund (ORF). H.C.L. was supported in part by the National Major Basic Research Project (2011CB925603) and the Natural Science Foundation of China (91221201 and 61234005).

APPENDIX: SIMULATIONS BY NONEQUILIBRIUM GREEN'S FUNCTION MODEL

Current and carrier densities as well as gain spectra of the V845 device were simulated with the NEGF method,[28] where the recent implementation described in Ref. 58 is used. As basis states, we use the Wannier functions of the envelope hamiltonian of the perfect QCL structure at zero bias. For this approach, the barrier height was ~12.5 meV smaller than in the RE model and a zero non parabolicity was assumed. Both features widely compensate and the resulting level spectrum is almost identical. Scattering effects from interface roughness, impurities, and phonons are treated with self-energies within the self-consistent Born approximation, while electron-electron interactions are appreciated by a self-consistently calculated mean field potential.

The current density has been calculated at different lattice temperatures as shown in Fig. 11. In these simulations, J_{max} is found at a total bias which is lower than the experimental bias of J_{max} (shifted by the Schottky bias drop) by ~1.8 V. The difference is slightly smaller for the first resonance peak. This contrasts with the RE method used in the main text, where no such shift was observed. We attribute the main part of the shift to the real parts of the self-energies and the mean field potential included in the NEGF model. Taking into account the real parts of the self-energies and the mean field potential provides different Wannier-Stark states as shown in Fig. 12(a). Here, the tunneling resonance between states *e* and *i* occurs at a field of 18.7 kV/cm, but the

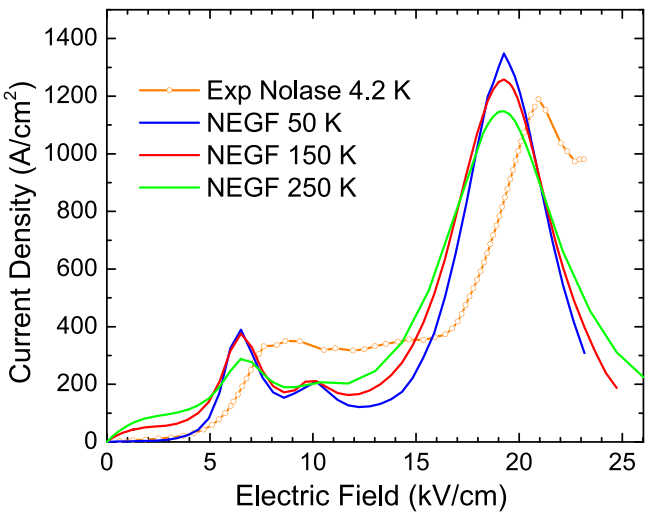

FIG. 11. Current densities at different lattice temperatures, calculated with the NEGF method. J_{max} is located at 19.3 kV/cm. The experimental curve of the non-lasing device, shown as an orange dotted line, was measured at 4.2 K for comparison.

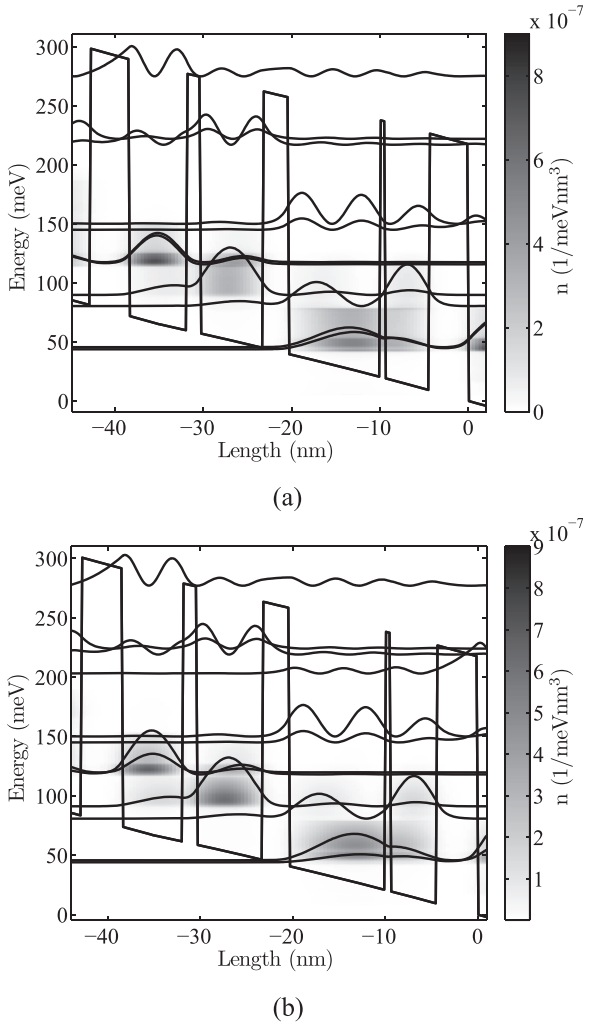

FIG. 12. Carrier densities at (a) 18.7 kV/cm and (b) 19.3 kV/cm. Current is peaked at the bias in (b), although the tunneling resonance is greater in (a).

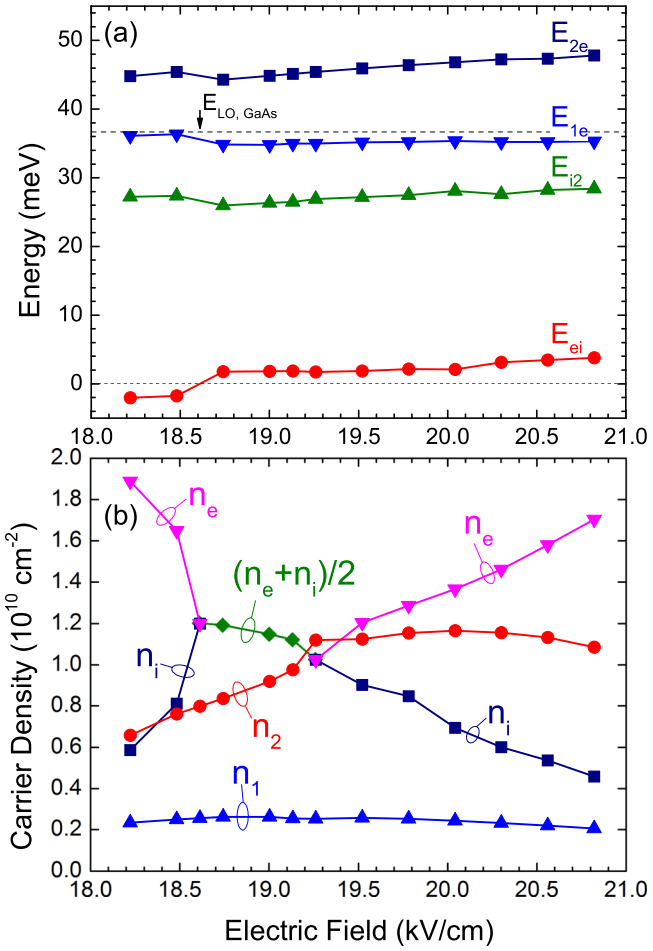

FIG. 13. (a) The detuning energy between extraction and injection states E_{ei}, the energy differences of the extraction E_{1e}, the injection E_{i2} and the energy spacing E_{2e} of the main leakage channel $2 \rightarrow e$. (b) Population densities of the injection n_i, upper laser n_2, lower laser n_1 and extraction n_e states. At electric fields where i and e are almost degenerate, the average value of n_e and n_i is shown.

injection energy $E_{i2} = 25.97$ meV deviates strongly from the phonon energy $E_{LO} = 36.7$ meV. (A detailed summary of the values is given in Fig. 13.) As a result, carriers accumulate in the injection state. Correspondingly, the current peak occurs for a slight detuning of E_i and E_e at 19.3 kV/cm (Fig. 12(b)). At higher fields, the detuning between E_i and E_e becomes significant and the current drops. Note that the population of the ULS is asymmetric with respect to the current peak, as the transition energy E_{2e} of the leakage channel $2 \rightarrow e$ becomes more detuned from E_{LO} with increasing field. This also results in a stronger inversion on the gain transition. The relevance of the mean-field can be quantified by solving Poisson's equation including the electron densities in Fig. 12(b) and the doping density. We find a maximum mean field potential of $\sim$1.8 meV (in the LLS well) and a minimum of ~ -0.7 meV in the doped well. This potential effectively raises e and the LLS, while it lowers i. This requires a lower bias for the $e-i$ tunneling resonance as compared to the case without mean field.

As the temperature increases, inversion decreases as a result of thermal backfilling from e to the LLS, as well as from the ULS to i. The first backfilling effect shows the importance of emptying the extraction state efficiently at the operating bias, whereas the latter shows the importance of matching the injection energy to E_{LO}. At fields below the first resonance peak, the current increases with temperature, whereas the peak itself decreases, in good agreement with the experiment (Fig. 4). In the region between the first resonance peak and J_{max}, the current also increases as in the experimental measurements. However, J_{max} decreases with temperature, whereas for the lasing device there is a decrease in current at low temperatures, but for higher temperatures the current drastically increases. The same effect is seen in the RE simulations with 5 states per period, and the NEGF with its 7 states per period thus confirms that this increase in J_{max} does not come from thermal excitations to higher states.

The gain spectra computed at different temperatures and for the electric field of J_{max} ($\sim$19.3 kV/cm) are shown in Fig. 14. Peak gain is achieved for $\nu = 2.5$ THz at J_{max}, which agrees much better with the experimental data than the RE results. This frequency corresponds to the difference in energy of the Wannier-Stark states responsible for lasing, and we thus conclude that the dispersive gain and depolarization shift included in the NEGF model do not play an

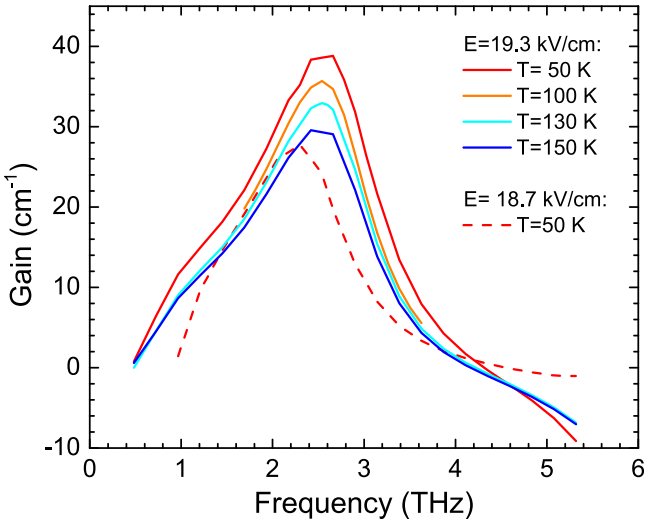

FIG. 14. The gain spectrum of the structure near the NDR and for different lattice temperatures. At 50 K, the gain spectrum at lower electric field is also plotted to show the red shift in the spectrum.

important role. The peak value of the gain decreases from 39 cm^{-1} at 50 K to 33 cm^{-1} at 130 K and finally, down to 30 cm^{-1} at 150 K. The full width at half maximum of the calculated gain ($\Delta\nu$) at 130 K is ~1.56 THz. At lower fields (see dashed line of Fig. 14), the gain goes down in magnitude, and the peak gain shifts to lower frequencies with a Stark shift ~0.45 THz/V, which is slightly higher than the experimental observation at 10 K (Fig. 6).

[1]B. S. Williams, Nature Photon. **1**, 517 (2007).
[2]C. Walther, M. Fischer, G. Scalari, R. Terazzi, N. Hoyler, and J. Faist, Appl. Phys. Lett. **91**, 131122 (2007).
[3]C. W. I. Chan, Q. Hu, and J. L. Reno, Appl. Phys. Lett. **101**, 151108 (2012).
[4]R. Kohler, A. Tredicucci, F. Beltram, H. E. Beere, E. H. Linfield, A. G. Davies, D. A. Ritchie, R. C. Iotti, and F. Rossi, Nature **417**, 156 (2002).
[5]S. Fathololoumi, E. Dupont, C. Chan, Z. Wasilewski, S. Laframboise, D. Ban, A. Mátyás, C. Jirauschek, Q. Hu, and H. C. Liu, Opt. Express **20**, 3866 (2012).
[6]H. Yasuda, T. Kubis, P. Vogl, N. Sekine, I. Hosako, and K. Hirakawa, Appl. Phys. Lett. **94**, 151109 (2009).
[7]T. Kubis, S. R. Mehrotra, and G. Klimeck, Appl. Phys. Lett. **97**, 261106 (2010).
[8]S. Kumar, C. W. I. Chan, Q. Hu, and J. L. Reno, Nat. Phys. **7**, 166 (2011).
[9]E. Dupont, S. Fathololoumi, Z. R. Wasilewski, G. Aers, S. R. Laframboise, M. Lindskog, S. G. Razavipour, A. Wacker, D. Ban, and H. C. Liu, J. Appl. Phys. **111**, 073111 (2012).
[10]M. Yamanishi, K. Fujita, T. Edamura, and H. Kan, Opt. Express **16**, 20748 (2008).
[11]S. Kumar, B. S. Williams, Q. Hu, and J. L. Reno, Appl. Phys. Lett. **88**, 121123 (2006).
[12]S. Kumar, Q. Hu, and J. L. Reno, Appl. Phys. Lett. **94**, 131105 (2009).
[13]M. A. Belkin, J. A. Fan, S. Hormoz, F. Capasso, S. P. Khanna, M. Lachab, A. G. Davies, and E. H. Linfield, Opt. Express **16**, 3242 (2008).
[14]M. Belkin, Q. J. Wang, C. Pflugl, A. Belyanin, S. Khanna, A. Davies, E. Linfield, and F. Capasso, IEEE Sel. Top. Quantum Electron. **15**, 952 (2009).
[15]A. Wacker, Appl. Phys. Lett. **97**, 081105 (2010).
[16]T. Liu, T. Kubis, Q. J. Wang, and G. Klimeck, Appl. Phys. Lett. **100**, 122110 (2012).
[17]M. Yamanishi, K. Fujita, N. Yu, T. Edamura, K. Tanaka, and F. Capasso, paper presented at Conference on Lasers and Electro-Optics, Baltimore, MD, USA, 1–6 May 2011.
[18]K. Fujita, M. Yamanishi, S. Furuta, K. Tanaka, T. Edamura, T. Kubis, and G. Klimeck, Opt. Express **20**, 20647 (2012).
[19]M. Yamanishi, K. Fujita, S. Furuta, K. Tanaka, T. Edamura, T. Kubis, and G. Klimeck, paper presented at International quantum cascades laser school and workshop, Baden, Austria, 2–6 September 2012.
[20]D. Indjin, P. Harrison, R. W. Kelsall, and Z. Ikonić, Appl. Phys. Lett. **82**, 1347 (2003).
[21]H. Callebaut, S. Kumar, B. S. Williams, Q. Hu, and J. L. Reno, Appl. Phys. Lett. **83**, 207 (2003).
[22]H. Callebaut, S. Kumar, B. S. Williams, Q. Hu, and J. L. Reno, Appl. Phys. Lett. **84**, 645 (2004).
[23]C. Jirauschek, G. Scarpa, P. Lugli, M. S. Vitiello, and G. Scamarcio, J. Appl. Phys. **101**, 086109 (2007).
[24]G. Scalari, R. Terazzi, M. Giovannini, N. Hoyler, and J. Faist, Appl. Phys. Lett. **91**, 032103 (2007).
[25]S. Kumar and Q. Hu, Phys. Rev. B **80**, 245316 (2009).
[26]E. Dupont, S. Fathololoumi, and H. C. Liu, Phys. Rev. B **81**, 205311 (2010).
[27]H. Callebaut and Q. Hu, J. Appl. Phys. **98**, 104505 (2005).
[28]S.-C. Lee and A. Wacker, Phys. Rev. B **66**, 245314 (2002).
[29]T. Kubis, C. Yeh, P. Vogl, A. Benz, G. Fasching, and C. Deutsch, Phys. Rev. B **79**, 195323 (2009).
[30]T. Schmielau and J. M. F. Pereira, Appl. Phys. Lett. **95**, 231111 (2009).
[31]H. Sakaki, IEEE J. Quantum Electron. **22**, 1845 (1986).
[32]F. Carosella, C. Ndebeka-Bandou, R. Ferreira, E. Dupont, K. Unterrainer, G. Strasser, A. Wacker, and G. Bastard, Phys. Rev. B **85**, 085310 (2012).
[33]C. Ndebeka-Bandou, F. Carosella, R. Ferreira, A. Wacker, and G. Bastard, Appl. Phys. Lett. **101**, 191104 (2012).
[34]S. Fathololoumi, E. Dupont, Z. R. Wasilewski, C. W. I. Chan, S. G. Razavipour, S. R. Laframboise, S. Huang, Q. Hu, D. Ban, and H. C. Liu, J. Appl. Phys. **113**, 113109 (2013).
[35]The figure of merit used during the GA optimization of this work was defined as a product of (gain(cm^{-1})-23), average transit time per period, and inverse of the superperiod length at 150 K. The value of 23 cm^{-1} for the waveguide loss might been slightly underestimated. The gain was calculated by using a 4-level rate equation model and by assuming $\Delta\nu =$ 1 THz for the full width at half maximum. A pure dephasing time of 0.35 ps was used. Even though during the GA optimization the gain was estimated for a 3D doping of 7×10^{15} cm^{-3}, at the last minute, before the MBE growth, it was finally increased to 9×10^{15} cm^{-3}.
[36]R. Terazzi, Ph.D. dissertation, ETH Zurich, 2012.
[37]T. Ando, J. Phys. Soc. Jpn. **54**, 2671 (1985).
[38]A. Mátyás, M. A. Belkin, P. Lugli, and C. Jirauschek, Appl. Phys. Lett. **96**, 201110 (2010).
[39]S. Fathololoumi, E. Dupont, S. G. Razavipour, S. R. Laframboise, G. Parent, Z. Wasilewski, H. C. Liu, and D. Ban, Semicond. Sci. Technol. **26**, 105021 (2011).
[40]M. V. Kisin, M. A. Stroscio, G. Belenky, and S. Luryi, Appl. Phys. Lett. **73**, 2075 (1998).
[41]T. Liu, K. E. Lee, and Q. J. Wang, Phys. Rev. B **86**, 235306 (2012).
[42]H. Willenberg, G. H. Döhler, and J. Faist, Phys. Rev. B **67**, 085315 (2003).
[43]R. Terazzi, T. Gresch, M. Giovannini, N. Hoyler, N. Sekine, and J. Faist, Nat. Phys. **3**, 329 (2007).
[44]Y. Yao, Z. Liu, A. Hoffman, K. Franz, and C. Gmachl, IEEE J. Quantum Electron. **45**, 730 (2009).
[45]In the limit of infinitely short lifetime of states i and 1, $n_2 + n_e = n_s$, which suggests that the population difference between the tunneling states above threshold, $n_e - n_i$, would be weakly voltage dependent in order to take into account the voltage dependence of the oscillator strength.
[46]S. G. Razavipour, E. Dupont, S. Fathololoumi, Z. R. Wasilewski, M. Lindskog, A. Wacker, S. R. Laframboise, and D. Ban, paper presented at International quantum cascades laser school and workshop, Baden, Austria, 2–6 September 2012.
[47]R. Terazzi, T. Gresch, A. Wittmann, and J. Faist, Phys. Rev. B **78**, 155328 (2008).
[48]R. C. Iotti, F. Rossi, M. S. Vitiello, G. Scamarcio, L. Mahler, and A. Tredicucci, Appl. Phys. Lett. **97**, 033110 (2010).
[49]M. S. Vitiello, L. Viti, L. Romeo, D. Ercolani, G. Scalari, J. Faist, F. Beltram, L. Sorba, and A. Tredicucci, Appl. Phys. Lett. **100**, 241101 (2012).
[50]S. Kumar, C. W. I. Chan, Q. Hu, and J. L. Reno, Appl. Phys. Lett. **95**, 141110 (2009).
[51]S. Kumar, Proc. SPIE **8496**, 849603 (2012).
[52]I. Bhattacharya, C. W. I. Chan, and Q. Hu, Appl. Phys. Lett. **100**, 011108 (2012).

[53]W. Freeman and G. Karunasiri, Phys. Rev. B **85**, 195326 (2012).
[54]P. Patimisco, G. Scamarcio, M. V. Santacroce, V. Spagnolo, M. S. Vitiello, E. Dupont, S. R. Laframboise, S. Fathololoumi, G. S. Razavipour, and Z. Wasilewski, Opt. Express **21**, 10172 (2013).
[55]A. Mátyás, R. Chashmahcharagh, I. Kovacs, P. Lugli, K. Vijayraghavan, M. A. Belkin, and C. Jirauschek, J. Appl. Phys. **111**, 103106 (2012).
[56]Device V843 was also fabricated at MIT with the same process as device B and it lased up to 141 K.
[57]B. Williams, S. Kumar, Q. Hu, and J. Reno, Opt. Express **13**, 3331 (2005).
[58]A. Wacker, M. Lindskog, and D. O. Winge, IEEE J. Sel. Top. Quantum Electron. **19**, 1200611 (2013).